RSC Advances

ROYAL SOCIETY OF CHEMISTRY

www.rsc.org/advances

Graphical Abstract

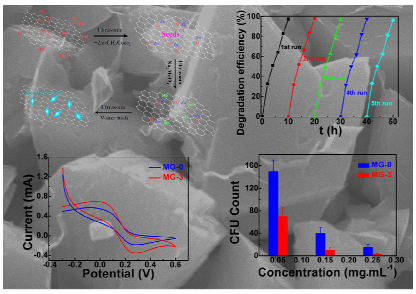

Well-dispersed, rhombus-shaped $ZnMoO_x$/RGO composites with multi-functionality have been fabricated employing an *in-situ*, ultrasonic-assisted approach.

Ultrasonic-assisted rational design of uniform rhombus-shaped $ZnMoO_x$ on graphene for advanced sunlight-driven photocatalysts, functionable supercapacitor electrodes, and antibacterial platforms

Shuying Dong[‡a], Limin Hu[‡a], Jinglan Feng[a], Yunqing Pi[a], Qilu Li[a], Yukun Li[a], Menglin Liu[a], Jingyu Sun[b1], Jianhui Sun[a2]

[a] *School of Environment, Henan Normal University, Key Laboratory for Yellow River and Huai River Water Environmental and Pollution Control, Ministry of Education, Henan Key Laboratory for Environmental Pollution Control, Xinxiang, Henan 453007, P. R. China*

[b] *Center for Nanochemistry (CNC), College of Chemistry and Molecular Engineering, Peking University, Beijing 100871, P. R. China*

[1] Corresponding author. E-mail: sunjy-cnc@pku.edu.cn (J.Y. Sun). Tel.: +86-10-62757157

[2] Corresponding author. E-mail: sunjh@htu.cn (J.H. Sun). Tel.: +86-373-3325971

[‡] These authors contributed equally to this work.

Abstract

To date, a growing interest has been devoted to fabricating graphene-metal oxide hybrid composites for a plethora of applications including photocatalysis. However, controllable synthesis of such composite materials by virtue of facile and rational routes still remains challenging. Herein, we report, for the first time, the design of an *in-situ*, ultrasonic-assisted growth strategy for the tailored production of well-dispersed, rhombus-shaped $ZnMoO_x$/reduced graphene oxide (RGO) composites. The resultant composites exhibit a superior and recyclable natural-sunlight-driven photocatalytic activity toward the degradation of Rhodamine B, where the highest photocatalytic degradation efficiency can be achieved for the $ZnMoO_x$/RGO composites with 3 wt% RGO dosage. In addition, the synthesized hybrids possess a high areal capacitance with a good cycling performance, as well as an interestingly noticeable antibacterial activity, offering special insights into the usage of such composites for a wide range of applications.

KEYWORDS: $ZnMoO_x$, RGO, natural sunlight, photocatalytic, Rhodamine B

1. Introduction

Graphene and relatives (e.g. reduced graphene oxide (RGO)) are of current interest for numerous applications due to their unique two-dimensional structure, large specific surface area, as well as remarkable electrical and mechanical properties, making them ideal supports for material integration.[1-4] Recent years have witnessed a growing attention in a plethora of graphene-based hybrid composites, giving rise to many novel application sectors ranging from solar light photocatalysis,[5] Li-ion batteries,[6] to H_2 generation[7] and high-performance supercapacitors[8]. In particular, combining RGO with metal oxide photocatalysts such as TiO_2,[9] $ZnSnO_3$,[10] $BiVO_4$,[11-14] Bi_2MoO_6,[15] and ZnO[16-18] to harness the excellent properties of graphene for advanced photocatalytic performance in pollutant degradation has been extensively demonstrated. Compared with solely inorganic photocatalysts, the involvement of RGO could contribute to an effective suppression of electron-hole recombination rates within the species, therefore boosting their practical usage in environmental protection.[19] Moreover, the RGO-metal oxide composites have been proven to be suitable for supercapacitor electrode, which mainly benefited from the unique planar morphology, high electronic conductivity, and good hydrophilicity of RGO.[20]

The formation of RGO-metal oxide composites can be realized *via* various methods including electro-deposition, co-precipitation, sol-gel strategy, and hydrothermal procedure. However, challenge still remains with regard to how to tailor the sizes, shapes, as well as uniform dispersions of inorganic architectures on RGO in a controllable manner during the

synthesis, since studies have revealed that uniform-shaped, well-dispersed nano/micro-sized crystals displayed superior performances especially in photocatalytic and electrochemical devices over the amorphous ones.[5] Another limitation hindering the practical usage of these hybrid composites is the multi-step, tedious and cost-ineffective synthetic protocols, which have been heavily employed to date to ensure the product quantity and quality. In this regard, facile and efficient routes, i.e. one-pot or *in-situ* synthesis, would be highly desirable.

Herein we report for the first time the design of an *in-situ* ultrasonic-assisted growth strategy to fabricate well-dispersed rhombus-shaped $ZnMoO_x$ microsized crystals on RGO, which allows facile and effective tuning of the graphene-based composites. The impetus for using $ZnMoO_x$ lies in the fact that this non-toxic material could form various shapes possessing excellent photoelectrochemical properties, widely applied in the field of catalysis, photoluminescence, photonics, and batteries,[21,22] where there has been no study so far on the integration of $ZnMoO_x$ with graphene to explore the natural-sunlight-driven photocatalytic properties of the composites. In this study, the growth and anchor of $ZnMoO_x$ particles on graphene and the reduction of GO sheets can be realized simultaneously. The resultant hybrid composite possesses a greatly recyclable natural-sunlight-driven photocatalytic activity towards degradation of Rhodamine B (RhB). It has been demonstrated that the hybrid with 3 wt% RGO dosage exhibits the highest RhB degradation efficiency (96.5%), which is far higher than that of the pure $ZnMoO_4$ sample (28.4%). Besides, the composite displays a high areal capacitance when functioned as a supercapacitor electrode. The antibacterial performance of the composite against *E. coli* has also been probed.

2. Experimental Section

2.1. Synthesis of $ZnMoO_x$/RGO composites

All the chemicals were analytical grade reagents and used as received without further purification. GO was synthesized from natural graphite powders according to the recipe described in our previous study.[10] Deionized water was used throughout this study.

Well-dispersed rhombus-shaped $ZnMoO_x$ microsized crystals were grown on RGO throughout a facile ultrasonic-assisted route (Fig. 1). One pot production could result in a weight of 500 mg, where the appearance of the powdered products is revealed in Fig. S1 (Electronic Supplementary Information). In a typical experimental process, a specific amount of GO was well dispersed in 40 mL distilled water by high frequency ultrasonic treatment for 60 min to get GO exfoliated. Then 2 mmol $Zn(CH_3COO)_2 \cdot 2H_2O$ was added into the above GO solution under continuous ultrasonic treatment for another 30 min to form "seeds" on the GO surface, after which the prepared solution was marked as solution A. Meanwhile, 2 mmol $Na_2MoO_4 \cdot 2H_2O$ was dissolved into 40 mL distilled water to form a transparent solution (solution B). Then B was added into A in a drop-by-drop manner at room temperature under continuous ultrasonic treatment for 120 min. After adding a specific volume of $N_2H_4 \cdot H_2O$, the suspension was placed into a water bath and maintained at 80 °C until it began to aggregate precipitate. After cooling down to room temperature, the $ZnMoO_x$/RGO composites were collected by filtration, rinsed with water for several times and then dried at 60 °C overnight. The weight ratio of GO to $Na_2MoO_4 \cdot 2H_2O$ were 0, 1%, 3%, 5%, 7% and 9%, and the obtained samples were labeled as

MG-0, MG-1, MG-3, MG-5, MG-7 and MG-9, respectively. The color of the synthesized composites by naked-eye observation was changed from white to dark grey as the RGO amount increased from MG-0 to MG-9.

(Figure 1)

2.2. Characterization

Powder X-ray diffraction (XRD) patterns were obtained on a Bruker-D8-AXS diffractometer system (Bruker Co., Germany) using Cu Kα radiation (λ = 0.15406 Å) at a scan rate of 0.02°/0.4 s to determine the crystal phases of the prepared $ZnMoO_x$/RGO composites. The morphologies of obtained materials were inspected by using a JSM-6390LV scanning electron microscopy (SEM). High resolution transmission electron microscopy (HRTEM) images and energy dispersive X-ray spectra (EDX) pattern were collected on a JEM-2100 electron microscopy. Fourier transform infrared (FT-IR) spectra were recorded using a FTIR Analyzer (Perkin-Elmer, Spectrum 400), and the KBr was served as a reference sample. The Raman spectra were acquired on a Horiba LabRAM HR-800 Raman spectroscopy using a 514 nm laser wavelength. The measurements of low-temperature N_2 adsorption were carried out by using a Micromeritics ASAP 2020 apparatus operating at -196 °C, where all the samples were degassed at 100 °C for 6 h prior to the measurement. The Ultraviolet-visible diffuse reflectance spectra were obtained from a UV-Vis-NIR spectrophotometer (Lambda 950, PerkinElmer). $BaSO_4$ was used as a reflectance standard, where the spectra were recorded at the wavelength range of 300-800 nm. The photoluminescence (PL) spectra of photocatalysts were recorded using a Fluorescence Spectrophotometer (FP-6500, Japan) equipped with a Xenon lamp at an excitation wavelength of

260 nm.

2.3. Evaluation of natural sunlight photocatalytic activity

The photocatalytic activities of the as-obtained $ZnMoO_x$/RGO composites were monitored through the photodegradation of RhB under natural sunlight irradiation. Photocatalytic reactions were carried out in a 250 mL borosilicate photochemical batch reactor. To ensure the sufficient illumination of the natural sunlight, all photocatalytic experiments were intentionally performed between 8:10 a.m. and 6:10 p.m. (the reaction time was 10 hr) in consecutive sunny days during the late September 2013. The ambient temperature was recorded. Moreover, the time-dependent light density of the natural sunlight was measured by using a digital Lux meter (UA1010B, Shenzhen UYIGAO E&T Co., China) during our experiments. In each experiment, a certain amount of catalyst was added into 200 mL RhB aqueous solution. No pH adjustment was used during the entire course of the photodegradation process. Prior to irradiation, the suspension was magnetically stirred (300 rpm) in the dark for 40 min to achieve an adsorption-desorption equilibrium between the RhB molecules and catalyst particles. During each photocatalytic experiment, 4 mL of the suspension was collected at predetermined time intervals for analysis.

The concentration of RhB was analyzed by measuring the absorption intensity at its maximum absorbance wavelength of λ = 553 nm using a UV-Vis spectrophotometer (UV-1700, SHIMADU) with a 1 cm path length spectrometric quartz cell, and was calculated from the calibration curve. The degradation efficiency of the RhB dye wastewater was determined according to the following equation:

$$\text{Degradation efficiency (\%)} = \frac{C_0 - C_t}{C_0} \times 100\% \quad (1)$$

where C_0 was the initial concentration of RhB (after the standing in the dark for 40 min) and C_t was the concentration of RhB at certain reaction time t (h).

2.4. Electrochemical measurements

The electrochemical measurements were performed using an electrochemical workstation (CHI-660D, China). Cyclic voltammetric (CV), electrochemical impedance spectroscopy (EIS) and chronopotentiometry were carried out using a conventional three-electrode system. In general, 1 mg of synthesized MG-0 or MG-3 was dropped on the carbon paper (~1.0×2.0 cm, effective area ~0.75 cm^2), which was used as a working electrode. The counter and reference electrodes were a platinum wire and saturated calomel electrode (SCE), respectively. A 300 W Xe lamp (CEL-S500/300, China) was used as the light source for the visible light irradiation in the photo-electrochemical analyses. The quartz electrolytic cell was filled with 10 mM $K_3Fe(CN)_6$ and 0.1 M KCl solution served as electrolyte for CV, 0.5 M Na_2SO_4 solution served as electrolyte for EIS and chronopotentiometry experiments, respectively. The areal capacitance (C_a) can be calculated from the galvanostatic charge-discharge curve according to the following equation:

$$C_a = \frac{I \Delta t}{S \Delta V} \quad (2)$$

where I is the discharge current, Δt is the discharge time, ΔV is the potential window during the discharge process, and S is the effective area of electrode.

2.5. Hydroxyl radical analysis in the photocatalytic process

A fluorescence technique with terephthalic acid (TPA) as a probe molecule was used to detect the formation of free hydroxyl radicals (˙OH) on the surface of the MG-0 and MG-3. 0.1 g of synthesized MG-0 or MG-3 was added into 200 mL mixed solution of 0.25 mM TPA and 1 mM NaOH, which was further applied by magnetically stirring for thorough dispersion. After irradiation under natural sunlight for 2 h, the reaction solution was centrifuged to measure the fluorescence spectra on a fluorescence spectrophotometer (FP-6500, Japan) excited at 315 nm.

2.6. Antibacterial performance

The antibacterial activity of the MG-0 and MG-3 against Escherichia coli (*E. coli*) was studied by a colony forming units (CFU) counting method. Test tube containing 10 mL growth medium were seeded with fresh *E. coli* at a concentration of 5×10^5 CFU per mL ($CFU\cdot mL^{-1}$). 0.005, 0.012, and 0.030 g MG-0 and MG-3 were added to the tubes, respectively, the control group contains neither MG-0 nor MG-3. The tubes were then incubated at 37 °C for 18 h. After incubation, media were diluted ten times and a 100 μL aliquot of the bacterial dispersion from the test and control group were transferred into the same solid beef extract peptone medium, respectively. The dispersion was uniformly coated using a coating stick, incubated without shaking to allow absorption for approximately 30 min at room temperature and then placed in an inverted culture incubator at 37 °C for 18 h. The number of colonies formed in each case was counted. The whole experiment was repeated three times to obtain a reasonable statistics.

3. Results and Discussion

3.1. Probing the effect of RGO dosages on the photocatalytic performances of $ZnMoO_x$/RGO

composites

Investigation of the photocatalytic activities of $ZnMoO_x$/RGO composites with different RGO dosages were carried out throughout the photodegradation of RhB under natural sunlight irradiation. To eliminate the effects of sunlight photolysis, control experiment by using 5 $mg \cdot L^{-1}$ RhB without any catalysts shows no significant change on the concentration of RhB occurred after 10 h irradiation, indicating that RhB was not prone to degradation by sunlight photolysis (black curve in Fig. 2). With the presence of pure $ZnMoO_x$ photocatalysts (MG-0), the degradation efficiency of RhB reaches 28.4% after 10 h sunlight irradiation (red curve in Fig. 2). In contrast, it has been found that the $ZnMoO_x$/RGO composites exhibit an apparent augmentation on the photodegradation efficiency, where even a small dosage (1 wt%) of RGO leads to an incredible enhancement in the photocatalytic performance (reaching 77.2%, blue curve in Fig. 2). Surprisingly, MG-3 displays a much greater photo-degradation performance with a corresponding degradation efficiency of 96.5% under the identical conditions (magenta curve in Fig. 2). However, further increasing the RGO dosages gives rise to decline in the photocatalytic activities. For instance, a sharp decrease in the degradation efficiency can be observed when RGO dosage is 5 wt% (olive curve in Fig. 2). This is in good agreement with the results reported in our and others' previous work, where RGO contents exerted a crucial effect on the photocatalytic activities of graphene-based hybrid photocatalysts.[12,23] Herein, MG-3 exhibits the highest natural-sunlight-driven photocatalytic activity compared to others, which has been selected as the representative for investigating the potentials (mainly in photocatalysis) of $ZnMoO_x$/RGO composites.

(Figure 2)

3.2. Characterizing the as-synthesized $ZnMoO_x$/RGO composites

SEM micrographs of pure $ZnMoO_x$ crystals (Fig. 3a, b) show uniform rhombus-shaped morphology with different sizes. Fig. 3c and d display the SEM observation of the $ZnMoO_x$/RGO composites (MG-3), where stratiform RGO sheets can be observed despite the low dosages. TEM image of MG-3 (Fig. 3e) further discloses the rhombus shape of an individual crystal with RGO coatings on the surface, accompanied by a representative HRTEM image of clearly-presented lattice fringes in Fig. 3f. The incorporated RGO sheets seem not detached or damaged during the TEM sample preparation, suggesting the formation of stable $ZnMoO_x$/RGO hybrids. The selected area electron diffraction (SAED) pattern in Fig. 3g reveals the poly-crystalline nature of $ZnMoO_x$ crystals. The bright spots shown in the SAED pattern could be indexed to (111), (333), and (440) of $ZnMoO_3$ phase as well as (-110), (2-11), (2-31), and (3-41) of triclinic $ZnMoO_4$ phase, respectively, where a corresponding fast Fourier transform (FFT) pattern (inset in Fig. 3g) further confirms the preferential crystal orientation of MG-3. The presence of C, O, Zn, and Mo elements within the composites is verified by the energy-dispersive X-ray (EDX) spectrum (Fig. 3h), with a quantitative analysis indicating that the atom ratio of Mo:Zn is 1:0.996. Raman spectra (Fig. 3i) show the characteristic peaks of $ZnMoO_4$ and $ZnMoO_3$ at 350 and 800-1000 cm^{-1}, respectively, indicating the formation of $ZnMoO_x$ crystals in both MG-0 and MG-3. It is noted that the inset in Fig. 3i shows the featured D (~1341 cm^{-1}) and G (~1586 cm^{-1}) bands of RGO for the MG-3, indicating that RGO is well decorated by $ZnMoO_x$ crystals.[24]

(Figure 3)

The XRD pattern (Fig. 4a) reveals the crystal phases of pure rhombus-shaped $ZnMoO_x$ (MG-0) and $ZnMoO_x$/RGO composite (MG-3), presenting the typical XRD diffraction character of a mixture phase of triclinic $ZnMoO_4$ (JCPDS file No. 35-0765) and $ZnMoO_3$ (No. 35-0019), which is in good agreement with the SAED results. No diffraction peak corresponding to graphite can be detected, suggesting that the dispersion of graphene sheets during the composite synthesis was well-maintained. However, high loading of RGO (e.g. MG-9) might accompany by the creation of reduced products such as MoO_3, since a relatively high amount of $N_2H_4 \cdot H_2O$ was used during the synthetic process. This is reflected by the fact that a new diffraction peak corresponding to MoO_3 (JCPDS file No. 35-0609)[25] can be detected in the XRD pattern of MG-9 (pink curve in Fig. S2, highlighting by a green circle). Moreover, it is interesting to observe the mixed phase of $ZnMoO_x$ products in this work. Spassky *et al.*[26] reported that the preparation of $ZnMoO_4$ single crystals were influenced by the level of thermal stress, where negligible fluctuations of the temperature could lead to a better homogeneity of the crystal. In our case, the continuous ultrasonic treatment during the synthesis would result in the steady increase of the system temperature, together with the consideration that the lattice stability of $AMoO_4$ was lower than that of its reduced form $AMoO_3$,[27] one could expect to observe the difference in phase formation in the fabricated composites.

FT-IR spectra of MG-O and MG-3 were recorded to identify the chemical structures of samples (Fig. 4b). The broad bands at 3280, 3173, 1618, and 1592 cm^{-1} are assigned to the OH stretching vibration and bending vibration of adsorbed water molecules on the samples.[28] Other

bands at approx. 1184, 979, 918, 840, and 554 cm^{-1} are attributed to the symmetric stretching modes (ν_1) of $(MoO_3)^{2-}$, the ν_1 stretching of Mo-O in bridging Mo-O-Mo linkages, the ν_1 stretching of $(MoO_4)^{2-}$ tetrahedrons, the asymmetric stretching (ν_3) vibration modes of Mo-O, and the asymmetric bending vibration modes (ν_4) of Mo-O, respectively,[29] further affirming the mixed phase of the as-synthesized $ZnMoO_x$ products. Moreover, the band at 433 cm^{-1} is most likely to be Zn-O stretching mode in zinc molybdates.[30]

The specific surface areas and porous structures of the MG-0 and MG-3 were investigated by nitrogen adsorption-desorption measurements, as shown in Fig. 4c. The nitrogen adsorption-desorption isotherm of MG-0 and MG-3 indicates that the hybrid composite possess a typical mesoporous structure (red curve in Fig. 4c) compared to the pure inorganic form (blue curve; almost no pores), with the value of the specific surface area of 2.5216 $m^2\ g^{-1}$ in contrast to that of the MG-0 (0.7581 $m^2\ g^{-1}$). It is well known that the mesoporous structure could be beneficial to the effective degradation of organic pollutants in water.[31] The enhanced adsorption behavior in the relatively high pressure (P/P_0) range observed for MG-3 is also a good indication of the presence of large amounts of mesopores within the sample. The corresponding pore size distribution curves (inset in Fig. 4c) show apparent disparity in the pore diameters between the MG-0 (18 nm) and MG-3 (230 nm), agreeing with SEM and TEM results. Such great surface areas with large pore sizes of composites would promote their photocatalytic applications, partially due to the fact that a larger specific surface area of photocatalysts could induce more surface active sites and function better in adsorbing dye molecules.

Optical absorption properties of materials play an important role in the photocatalysis,

especially with regard to the visible light photodegradation of organic contaminants.[32] Fig. 4d displays the UV-vis DR spectra of MG-0 and MG-3, where the pure $ZnMoO_x$ (MG-0) exhibits a strong absorption in the UV light region but an almost vanished absorption signal in visible light region. The double-step shape of the spectrum (blue curve in Fig. 4d) is consistent with above-presented results showing that the MG-0 is indeed a mixture phases of $ZnMoO_4$ and $ZnMoO_3$. In contrast, the dosage of RGO (with different loadings) could improve the visible light absorption of the materials, where all the $ZnMoO_x$/RGO composites exhibit strong absorption characters in the whole UV-vis range (red curve in Fig. 4d and Fig. S3). It is noted that MG-9 sample exhibits an absorption peak at 500-600 nm (wheat colored line in Fig. S3), which is quite different from that of other samples. As aforementioned, our synthetic route of MG-9 could give rise to the formation of MoO_3 (Fig. S2), which could contribute to the shoulder absorption peak in the wavelength range of 500-600 nm, consistent with the observation reported by He *et al.*[25] The steep shapes of the spectra indicate that the visible-light absorption is due to the transition from the band-gap transition. The better optical absorption behavior of the composites over the visible light range could lead to their augmented sunlight-driven photocatalytic activities for the degradation of RhB-contained wastewater.

Additionally, the band-gap energy (E_g) of prepared products can be estimated from a plot depicting $(Ahv)^2$ *versus* hv, where A, h, and v represent the absorption coefficient, Planck constant, and the incident light frequency, respectively. The intercept of the tangent to the x axis gives rise to a good approximation of the E_g for the pure $ZnMoO_x$ as well as the $ZnMoO_x$/RGO composites (Fig. 4e and Fig. S4). The estimated E_g values of the obtained products have been

measured to be approx. 3.82 eV (MG-0), 3.22 eV (MG-1), 2.81 eV (MG-3), 2.95 eV (MG-5), 2.98 eV (MG-7) and 3.20 eV (MG-9), respectively. Apparently, MG-3 displays the highest visible-light absorption intensity but possesses the lowest band-gap energy, suggesting that the advanced photocatalytic activities of $ZnMoO_x$/RGO composites might be partially attributed to the light absorption enhancing and band-gap narrowing.

It is well known that the photoluminescence (PL) is a facile technique to study the photochemical properties of semiconductor materials, where the PL emission intensity is proportional to the opportunity of the recombination of charge carriers. Fig. 4f shows the PL spectra of the as-synthesized MG-0 and MG-3. Both curves exhibit evident PL signals with similar curve shapes, where the strong peaks centering at approx. 520 nm correspond to the green light region. Herein the emission peak is close to that reported for triclinic $ZnMoO_4$ (centering at 530 nm), which originates from the radiative annihilation of self-trapped excitons on MoO_4^{2-} complexes.[33] Notably, the integration of RGO strongly suppresses the PL emission intensity of the composites, which might be due to the fact that an efficient charge separation process occurred *via* direct electron transfer from $ZnMoO_x$ to RGO through the chemical bonding of Zn-Mo-O-C.

(Figure 4)

Fig. 5a shows CV curves of MG-0 and MG-3 obtained at scan rate of 10 $mV \cdot S^{-1}$ in a solution of 10 mM $K_3Fe(CN)_6$ and 0.1 M KCl, which usually serves as a benchmark for investigating electrocatalytic properties of different carbon materials.[34] With potential windows ranging from -0.3 to 0.6 V, both the electrodes exhibit apparently reversible voltammograms,

where the $Fe(CN)_6^{3-}$/ $Fe(CN)_6^{4-}$ redox pairs is highly resolved at the MG-3 electrode at which the redox current is 1.5-fold as great as that at the MG-0 electrode. As depicted, the increased redox current and peak-to-peak separation can be observed, indicating that the MG-3 electrode fosters a faster electron transfer.

EIS analysis serves as an informative technique to evaluate the charge transport in the electrochemical interfacial reactions.[35] Fig. 5b shows the EIS response of the MG-0 and MG-3 under visible light irradiation. The radius of the arc on the EIS Nyquist plot denotes the reaction rate occurring at the surface of the electrode. Apparently, the radius for the MG-3 (red curve) decreases significantly compared with that of the MG-0 (blue curve), indicating that both the solid state interface layer resistance and charge-transfer resistance have greatly declined by the introduction of RGO. The electron accepting and transporting properties of graphene within the MG-3 contribute to an effective separation of photo-generated electron-hole pairs, thereby leading to a faster interfacial charge transfer between the electron donor/acceptor, which will in turn, results in an enhancement in the photocatalytic oxidation rate. Herein the EIS results reveal that RGO might act as an electron acceptor in the hybrid composites to suppress charge recombination, hence giving rise to a higher photocatalytic response.

Hydroxyl radical (˙OH) trapping experiment by virtue of a fluorescence technique by using terephthalic acid (TPA) as a probe molecule was conducted, since ˙OH has been considered as an important reaction species in the photocatalytic degradation of contamination.[36] In this regard, TPA reacts readily with ˙OH to produce a highly fluorescent product, 2-hydroxyterephthalic acid, whose PL peak intensity is in proportion to the amount of ˙OH produced in water. As shown in

Fig. 5c, the peak intensity of MG-3 is greater than that of MG-0, suggesting the formation rate of ˙OH on the surface of MG-3 is much higher than that of MG-0. Additionally, there is no radical formation in the blank test (no photocatalyst) under natural sunlight irradiation.

(Figure 5)

Based on the above results, a conclusion could be drawn that the enhancement of photocatalytic activity of MG-3 might be due to the improved light absorption, augmented specific surface area, as well as advanced electronic conductivity when binding with RGO. With the presence of RGO, the photo-generated electrons in the conduction band of the $ZnMoO_x$ can be channeled into RGO, therefore suppressing the recombination of the photo-generated electron-hole pairs and leading to an effective charge separation and stabilization. Along with the generated holes, these electrons could further contact with H_2O or O_2 to produce hydroxyl (˙OH) or superoxide ($˙O_2^-$) radicals responsible for the detected great photocatalytic capacity of hybrids (Fig. 6). The complex reaction mechanism for the photodegradation process of RhB is still under consideration.

(Figure 6)

3.3. Investigating the photocatalytic activities and recycle performances of the representative MG-3 photocatalyst

3.3.1 Photocatalytic degradation of RhB

The sunlight-driven photocatalytic activity of representative MG-3 was probed by monitoring the photo-degradation of RhB under natural sunlight irradiation. To seek the optimum conditions for photocatalysis, the effects of photocatalyst dosage (Fig. 7a) and initial

concentration of pollutant (Fig. 7b) have been investigated. It can be observed from Fig. 7a that the degradation efficiency of RhB (with a concentration of 5 $mg \cdot L^{-1}$) rises from 65% to 98% with increasing dosages of MG-3 from 0.05 to 0.1 g. This observation can be explained by the fact that the amounts of photo-generated reactive species correspondingly increase by adding more catalyst. However, further increasing the dosage of MG-3 from 0.1 to 0.2 g lead to the decrease of degradation efficiency down to 73.2% (0.2 g) compared to 98% (0.1 g), which might be due to the fact that too much catalyst dosage could exert both steric and scattering effect on the light utilization of catalyst particles.

With respect to the effect of initial concentration of RhB (2.5-10 $mg \cdot L^{-1}$), it can be found that the degradation efficiency of RhB decreases from 99.8% to 71.1% with the initial dye concentration increases from 2.5 to 10 $mg \cdot L^{-1}$ (Fig. 7b). It is apparent that the higher concentration of dye would sooner consume the reactive radicals generated from the fixed dosage of the photocatalyst and might also decrease the light utilization rate by MG-3, resulting in the decrease of photodegradation efficiency. Therefore, an optimal concentration of RhB was set at 5 $mg \cdot L^{-1}$.

3.3.2 Recycle performances of MG-3 photocatalyst

The recycle experiments were performed to evaluate the photocatalytic repeatability and stability of synthesized MG-3 under natural sunlight irradiation. The degradation efficiency of RhB during each cycle (at the duration of 10 h) can reach 98% (in comparison with that of MG-0 at ~25% under identical conditions). After five cycling runs of photodegradation of RhB, the photocatalytic capacity of MG-3 has not exhibited any significant loss (Fig. 7c). The MG-3

composites employed in the recycle tests were further characterized by XRD and FT-IR after the experiments. The corresponding XRD pattern (Fig. 7d) and FT-IR spectrum (Fig. 7e) reveal that there is no observable change in the crystal structures as well as chemical structures of the photocatalysts, indicating that the MG-3 is structurally and chemically stable over prolonged irradiation time.

(Figure 7)

3.4. Monitoring the capacitive and antibacterial properties of the representative MG-0 and MG-3

In addition to functioning as recyclable photocatalysts for pollutant degradation, the $ZnMoO_x$/RGO composites enable the design of high-performance supercapacitor electrodes as well as antibacterial platforms. The areal capacitance of the composite electrodes was measured by galvanostatic charge-discharge methods, where the typical curves of MG-0 and MG-3 electrodes collected at a current density of 0.1 mA cm^{-2} are displayed in Fig. 8a. In this regard, the areal capacitance of MG-3 supercapacitors can be calculated to be 1.02 mF cm^{-2}, the value of which is superior to that for other Zn-based (0.27 mF cm^{-2} at 0.05 mA cm^{-2}) supercapacitor[37] and is comparable with the value reported for a carbon-based (0.4~2 mF cm^{-2}) supercapacitor.[38] Moreover, the cyclic performance of the MG-3 electrode was also targetedly examined by galvanostatic charge/discharge test for 1,000 cycles since the stability and reversibility of an electrode material is of great importance to the practical application of supercapacitors. It can be observed that the capacitance retention ratio of the MG-3 electrodes calculated from charge-discharge curve exhibits little decay during the test, suggesting that such samples possess

good stability (Fig. 8b).

More interestingly, the antibacterial activities of the fabricated $ZnMoO_x$/RGO composites were detected in our investigation, where the antibacterial performances against *E. coli* were determined by colony forming units (CFU) enumeration method (the appearance of sample shown in Fig. S5). The statistics in Fig. 8c clearly disclose that both MG-0 and MG-3 have good antibacterial activity against *E. coli*. In particular, the enhanced antibacterial activity of $ZnMoO_x$ in combination with RGO (MG-3) is reflected by the fact that nearly 100% reduction of CFU counts of *E. coli* in the medium occurs when increasing the concentration of composites. In contrast, the control sample without the presence of either MG-0 or MG-3 shows unrestricted *E. coli* growth behavior with 460 ± 60 CFU in the medium (no antibacterial activity). Such performance of the hybrids might pave the way for the development of antibacterial coatings or platforms.

(Figure 8)

4. Conclusions

In summary, we have devised an *in-situ*, ultrasonic-assisted growth strategy for the controllable synthesis of well-dispersed, rhombus-shaped $ZnMoO_x$/RGO composites. This method allows the one-pot, facile synthesis of desired hybrid products at a large scale with the aid of simple ultrasonic process, realizing the effective integration of $ZnMoO_x$ crystals with RGO. The novel 3D shaped metal oxide-2D graphene hybrids afford high surface area, improved light absorption feature, and good electronic conductivity, giving rise to the superior and recyclable

natural-sunlight-driven photocatalytic activities. Furthermore, we have demonstrated that such composites exhibit a high areal capacitance with a good cycling performance. More interestingly, we have found that the as-fabricated composites offer insights into the development of antibacterial platforms due to its remarkable antibacterial activities. This synthesis method represents a rational design of graphene-based hybrid materials with promising applications for photocatalysis, electrochemical catalysis, supercapacitors, and antibacterial agents.

Acknowledgements

The authors are grateful for the financial support from the Basic Scientific and Technological Frontier Project of Henan Province, PR China (Grant Nos. 132330410138, 102300410098 and 122300410293), the Key Science and Technology Program of Henan Province, PR China (Grant Nos. 122102310486 and 132102210129). The authors also would like to thank the Innovation Scientists and Technicians Troop Construction Projects of Henan Province, the Plan for Scientific Innovation Talent of Henan Province (Grant No. 134200510014), and the Fostering Foundation of Henan Normal University for the Author of National Excellent Ph.D. Dissertation, PR China (Grant No. 01333900011).

References

1 X. Huang, X. Qi, F. Boey and H. Zhang, *Chem. Soc. Rev.,* 2012, **41**, 666-686.

2 K. Novoselov, A. Geim, S. Morozov, D. Jiang, Y. Zhang, S. Dubonos, I. Grigorieva and A. Firsov, *Science,* 2004, **306**, 666-669.

3 J. Sun, T. Gao, X. Song, Y. Zhao, Y. Lin, H. Wang, D. Ma, Y. Chen, W. Xiang, J. Wang, Y. Zhang and Z. Liu, *J. Am. Chem. Soc.,* 2014, **136**, 6574-6577.

4 H. Wang, H. Casalongue, Y. Liang and H. Dai, *J. Am. Chem. Soc.,* 2010, **132**, 7472-7477.

5 Q. Xiang, J. Yu and M. Jaroniec, *Chem. Soc. Rev.,* 2012, **41**, 782-796.

6 J. Liang, Y. Liu, L. Guo and L. Li, *RSC Adv.*, 2013, **3**, 11489-11492.

7 F. Meng, J. Li, S. Cushing, M. Zhi and N. Wu, *J. Am. Chem. Soc.,* 2013, **135**, 10286-10289.

8 Y. Huang, J. Liang and Y. Chen, *Small,* 2012, **8**, 1805-1834.

9 X. Liu, L. Pan, T. Lv, G. Zhu, T. Lu, Z. Sun and C. Sun, *RSC Adv.*, 2011, **1**, 1245-1249.

10 S. Dong, J. Sun, Y. Li, C. Yu, Y. Li and J. Sun, *Appl. Catal. B: Environ.,* 2014, **144**, 386-393.

11 Y. Ng, A. Iwase, A. Kudo and R. Amal, *J. Phys. Chem. Lett., 2010,* **1**, 2607-2612.

12 S. Dong, Y. Cui, Y. Wang, Y. Li, L. Hu, J. Sun and J. Sun, *Chem. Eng. J.,* 2014, **249**, 102-110.

13 Y. Li, S. Dong, Y. Wang, J. Sun, Y. Li, Y. Pi, L. Hu and J. Sun, *J. Mol. Catal. A: Chem.,* 2014, **387**, 138-146.

14 Y. Yan, S. Sun, Y. Song, X. Yan, W. Guan, X. Liu and W. Shi, *J. Hazard. Mater.,* 2013, **250-251**, 106-114.

15 P. Wang, Y. Ao, C. Wang, J. Hou and J. Qian, *Carbon,* 2012, **50**, 5256-5264.

16 T. Xu, L. Zhang, H. Cheng and Y. Zhu, *Appl. Catal. B: Environ.,* 2011, **101**, 382-387.

17 Y. Liu, Y. Hu, M. Zhou, H. Qian and X. Hu, *Appl. Catal. B: Environ.,* 2012, **125**, 425-431.

18 S. Dong, Y. Li, J. Sun, C. Yu, Y. Li and J. Sun, *Mater. Chem. Phys.,* 2014, **145**, 357-365.

19 H. Chang and H. Wu, *Energ. Environ. Sci.,* 2013, **6**, 3483-3507.

20 Y. He, W. Chen, X. Li, Z. Zhang, J. Fu, C. Zhao and E. Xie, *ACS Nano.,* 2013, **7**, 174-182.

21 Y. R. Jiang, W. W. Lee, K. T. Chen, M. C. Wang, K. H. Chang and C. C. Chen, *J. Taiwan. Inst. Chem. E.,* 2014, **45**, 207-218.

22 D. A. Spassky, A. N. Vasil'ev, I. A. Kamenskikh, V. V. Mikhailin, A. E. Savon, Y. A. Hizhnyi, S. G. Nedilko and P. A. Lykov, *J. Phys-condens. Mat.,* 2011, **23**, 365501.

23 P. Madhusudan, J. Yu, W. Wang, B. Cheng and G. Liu, *Dalton. Trans.,* 2012, **41**, 14345-14353.

24 Y. Keereeta, T. Thongtem and S. Thongtem, *Superlattice. Microstruct.,* 2014, **69**, 253-264.

25 Y.M He, L.H. Zhang, X.X. Wang, Y. Wu, H.J. Lin, L.H. Zhao, W.Z. Weng, H.L. Wan and M.H. Fan, *RSC Adv.*, 2014, **4**, 13610-13619.

26 D.A. Spassky, V.V. Mikhailin, A.E. Savon, E.N. Galashov, V.N. Shlegel and Y.V. Vasiliev, *Opt. Mater.,* 2012, **34**, 1804-1810.

27 D. Logvinovich, M.H. Aguirre, J. Hejtmanek, R. Aguiar, S.G. Ebbinghaus, A. Reller and A. Weidenkaff, *J. Solid State Chem.,* 2008, **181**, 2243-2249.

28 D. Li, R. Shi, C. Pan, Y. Zhu and H. Zhao, *CrystEngComm.,* 2011, **13**, 4695-4700.

29 Y. Keereeta, T. Thongtem and S. Thongtem, *Mater. Lett.,* 2012, **68**, 265-268.

30 C. Pholnak, C. Sirisathitkul and D. J. Harding, *J. Phys. Chem. Solids,* 2011, **72**, 817-823.

31 S. Liu, C. Liu, W. Wang, B. Cheng and J. Yu, *Nanoscale,* 2012, **4**, 3193-3200.

32 X. Bai, L. Wang, R. Zong, Y. Lv, Y. Sun and Y. Zhu, *Langmuir,* 2013, **29**, 3097-3105.

33 Y. Liang, P. Liu, H. B. Li and G. W. Yang, *Cryst. Growth. Des.,* 2012, **12**, 4487-4493.

34 W. Zhao, Y. Wang, Y. Yang, J. Tang and Y. Yang, *Appl. Catal. B: Environ.,* 2012, **115-116**, 90-99.

35 D. Li, R. Shi, C. Pan, Y. Zhu and H. Zhao, *CrystEngComm.,* 2011, **13**, 4695-4700.

36 H. Huang, D. Li, Q. Lin, W. Zhang, Y. Shao, Y. Chen, M. Sun and X. Fu, *Environ. Sci. Technol.,* 2009, **43**, 4164-4168.

37 P. Yang, X. Xiao, Y. Li, Y. Ding, P. Qiang, X. Tan, W. Mai, Z. Lin, W. Wu, T. Li, H. Jin, P. Liu, J. Zhou, C. P. Wong and Z. L. Wang, *Acs Nano.,* 2013, **7**, 2617-2626.

38 D. Pech, M. Brunet, H. Durou, P. Huang, V. Mochalin, Y. Gogotsi, P. L. Taberna and P. Simon, *Nat. Nanotechnol*., 2010, **5**, 651-654.

Figures List:

Fig. 1. Schematic illustration of the *in-situ* ultrasonic-assisted growth strategy toward well-dispersed rhombus-shaped $ZnMoO_x$ microsized crystals on RGO.

Fig. 2. Comparison of the degradation efficiencies of the RhB-contained wastewater by using the as-synthesized $ZnMoO_x$/RGO composites with different RGO loadings as photocatalysts under natural sunlight irradiation.

Fig. 3. (a,b) SEM images of pure rhombus-shaped $ZnMoO_x$ microcrystals (MG-0). Scale bar: 1 μm. (c,d) SEM images of $ZnMoO_x$/RGO composites (MG-3). Scale bar: 1 μm. (e,f) Low-magnified (e) and high-resolution (f) TEM images of MG-3. Scale bar: (e) 500 nm; (f) 2 nm. (g) SAED pattern of MG-3 with the corresponding FFT pattern as the inset. (h) EDX spectrum of the MG-3 sample. (i) Raman spectra of MG-0 and MG-3, with the inset showing the specific features of RGO within the composites.

Fig. 4. (a) XRD pattern, (b) FTIR spectra of pure $ZnMoO_x$ (MG-0) and $ZnMoO_x$/RGO composites (MG-3). (c) Nitrogen adsorption-desorption isotherms of MG-0 and MG-3 and corresponding pore size distribution curves (inset). (d) UV-vis DR spectra and (e) the relationship between $(Ahv)^2$ and the photon energy (hv) of MG-0 and MG-3. (f) PL spectra of MG-0 and MG-3.

Fig. 5. (a) CV curves of the MG-0 and MG-3 electrodes in a solution of 10 mM $K_3Fe(CN)_6$ and 0.1 M KCl at scan rate of 10 mV S^{-1} under visible light irradiation. (b) EIS curves of the MG-0 and MG-3 electrodes in a solution of 0.1 M Na_2SO_4 under visible light irradiation. (c) PL spectra of the MG-0 and MG-3 in TPA solution after 2 h sunlight irradiation, revealing the ample formation rate of hydroxyl radicals for MG-3.

Fig. 6. Schematic illustration of the mechanism of charge transfer and photocatalytic process of RhB degradation over $ZnMoO_x$/RGO composites under natural sunlight irradiation.

Fig. 7. The degradation efficiencies of the RhB solution by varying (a) the MG-3 dosage ([RhB] = 5 mg L^{-1}) and (b) the initial concentration of RhB ([MG-3] = 0.1 g) under natural sunlight irradiation. (c) Cycling photo-degradation of RhB-contained solution ([RhB] = 5 mg L^{-1}) using MG-3 (0.1 g) under natural sunlight irradiation. (d) XRD pattern and (e) FT-IR spectrum of the MG-3 experiencing the recycle experiment.

Fig. 8. (a) Galvanostatic charge/discharge curves of MG-0 and MG-3. (b) Cycle performance of the MG-3 measured at a current density of 0.1 mA cm^{-2}. The inset in (b) is the corresponding galvanostatic charge/discharge curve. (c) CFU counts of *E. coli* by using MG-0 and MG-3 as the culture medium.

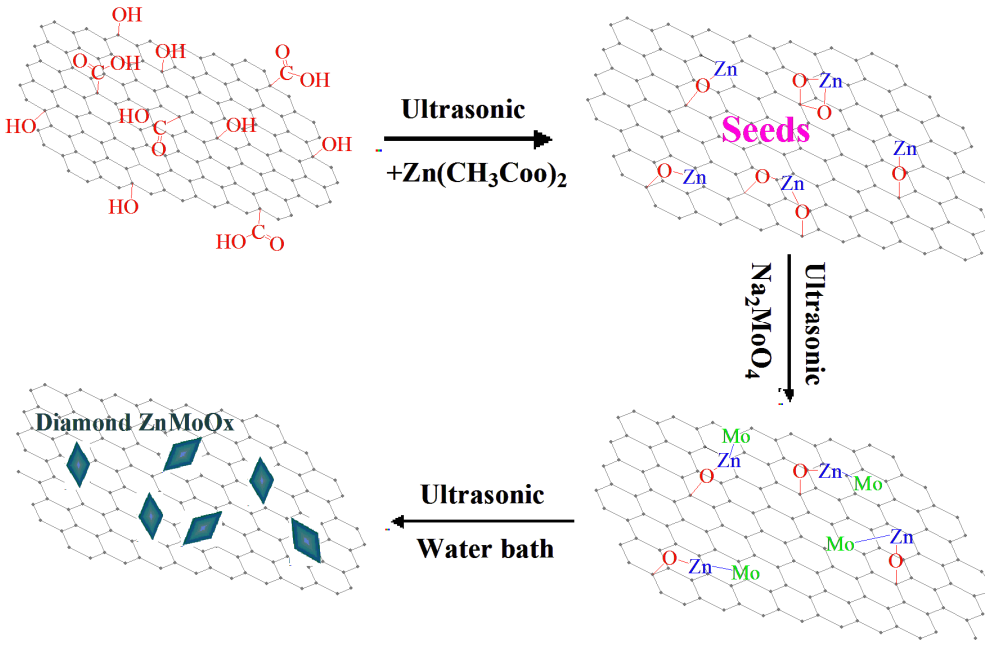

Fig. 1. Schematic illustration of the *in-situ* ultrasonic-assisted growth strategy toward well-dispersed rhombus-shaped $ZnMoO_x$ microsized crystals on RGO.

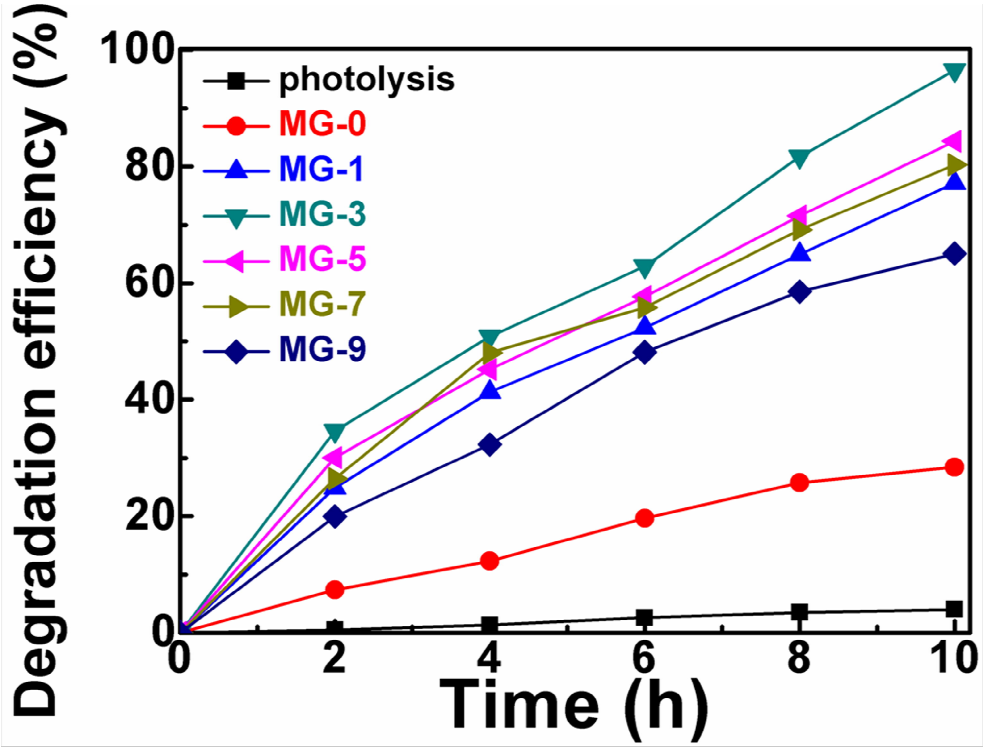

Fig. 2. Comparison of the degradation efficiencies of the RhB-contained wastewater by using the as-synthesized $ZnMoO_x$/RGO composites with different RGO loadings as photocatalysts under natural sunlight irradiation.

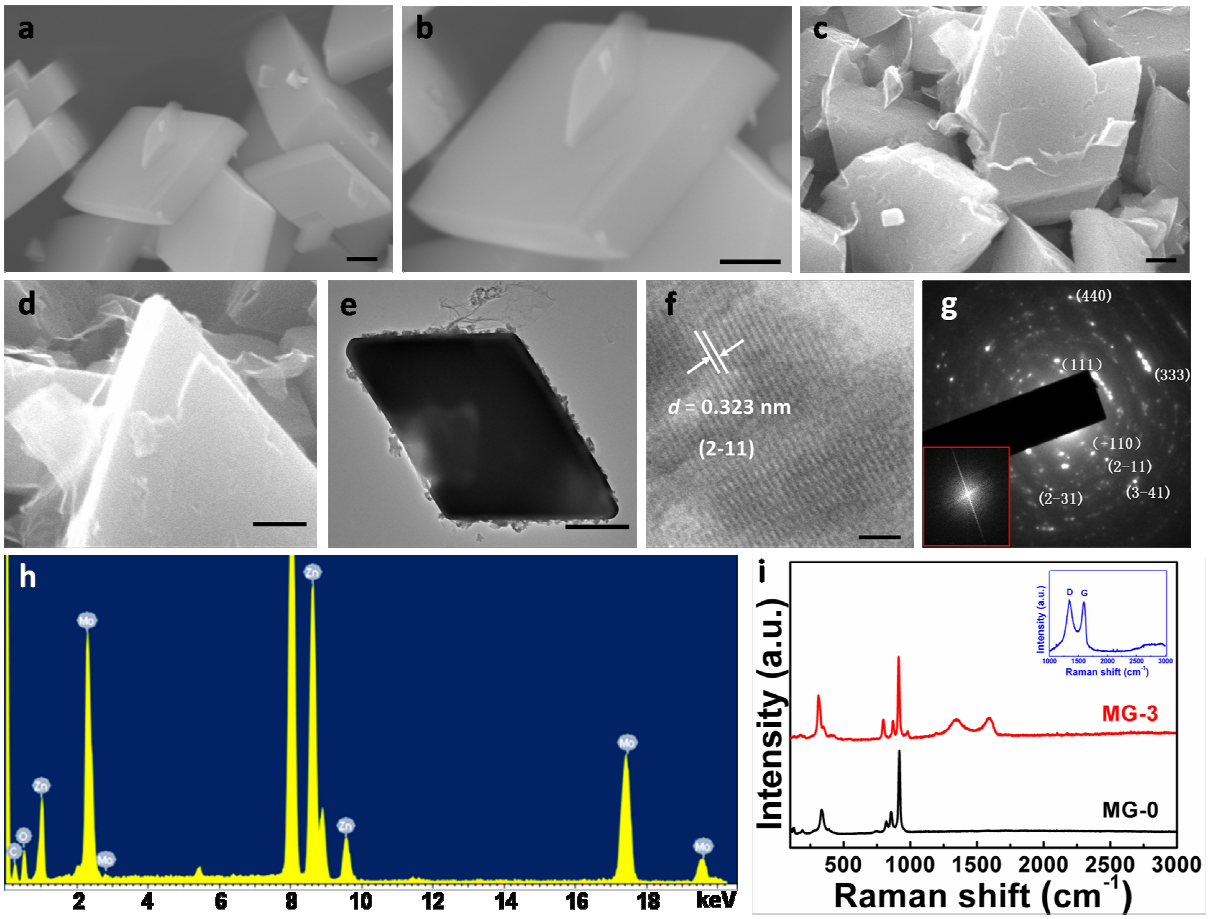

Fig. 3. (a,b) SEM images of pure rhombus-shaped $ZnMoO_x$ microcrystals (MG-0). Scale bar: 1 μm. (c,d) SEM images of $ZnMoO_x$/RGO composites (MG-3). Scale bar: 1 μm. (e,f) Low-magnified (e) and high-resolution (f) TEM images of MG-3. Scale bar: (e) 500 nm; (f) 2 nm. (g) SAED pattern of MG-3 with the corresponding FFT pattern as the inset. (h) EDX spectrum of the MG-3 sample. (i) Raman spectra of MG-0 and MG-3, with the inset showing the specific features of RGO within the composites.

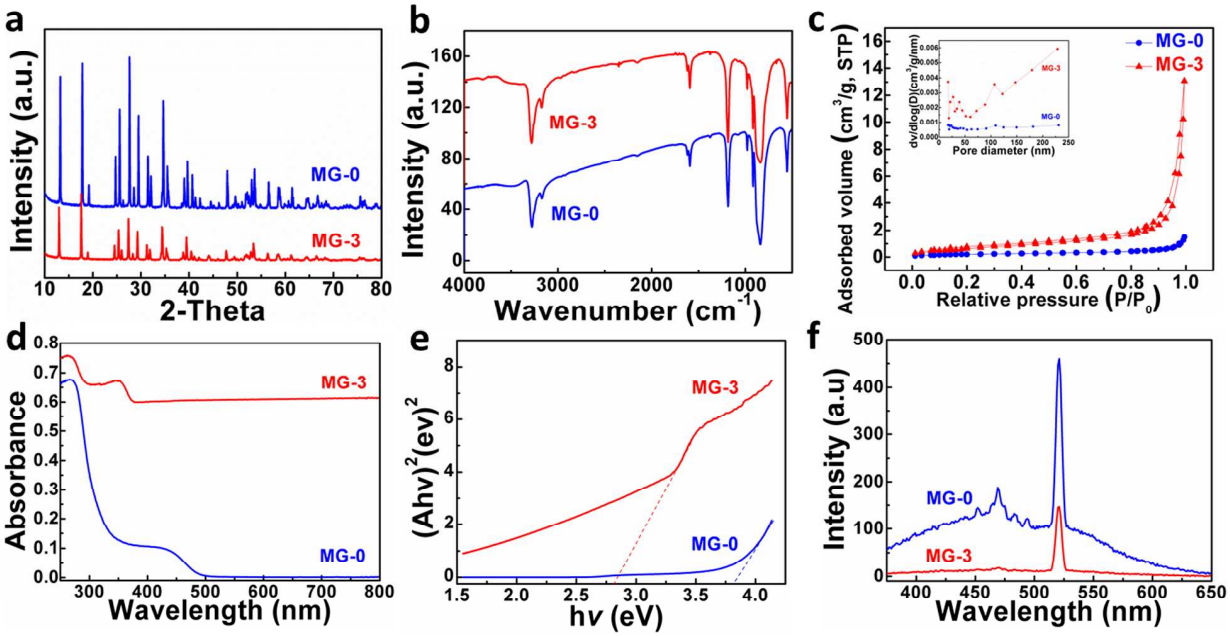

Fig. 4. (a) XRD pattern, (b) FTIR spectra of pure $ZnMoO_x$ (MG-0) and $ZnMoO_x$/RGO composites (MG-3). (c) Nitrogen adsorption-desorption isotherms of MG-0 and MG-3 and corresponding pore size distribution curves (inset). (d) UV-vis DR spectra and (e) the relationship between $(Ahv)^2$ and the photon energy (hv) of MG-0 and MG-3. (f) PL spectra of MG-0 and MG-3.

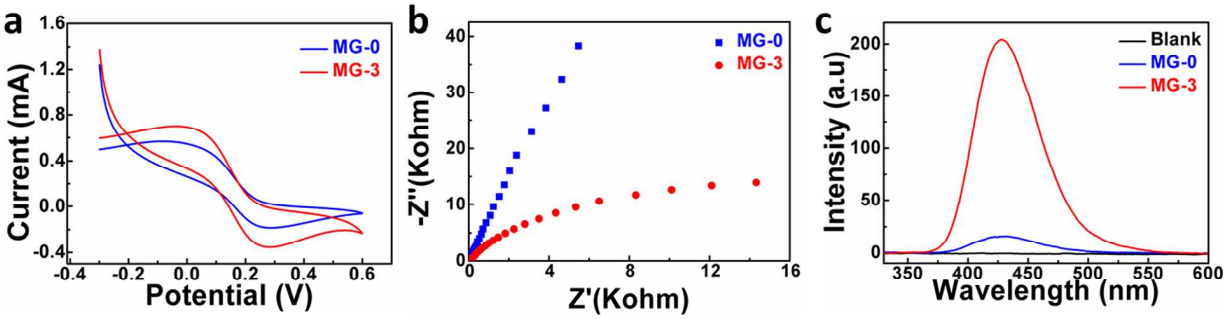

Fig. 5. (a) CV curves of the MG-0 and MG-3 electrodes in a solution of 10 mM $K_3Fe(CN)_6$ and 0.1 M KCl at scan rate of 10 mV S^{-1} under visible light irradiation. (b) EIS curves of the MG-0 and MG-3 electrodes in a solution of 0.1 M Na_2SO_4 under visible light irradiation. (c) PL spectra of the MG-0 and MG-3 in TPA solution after 2 h sunlight irradiation, revealing the ample formation rate of hydroxyl radicals for MG-3.

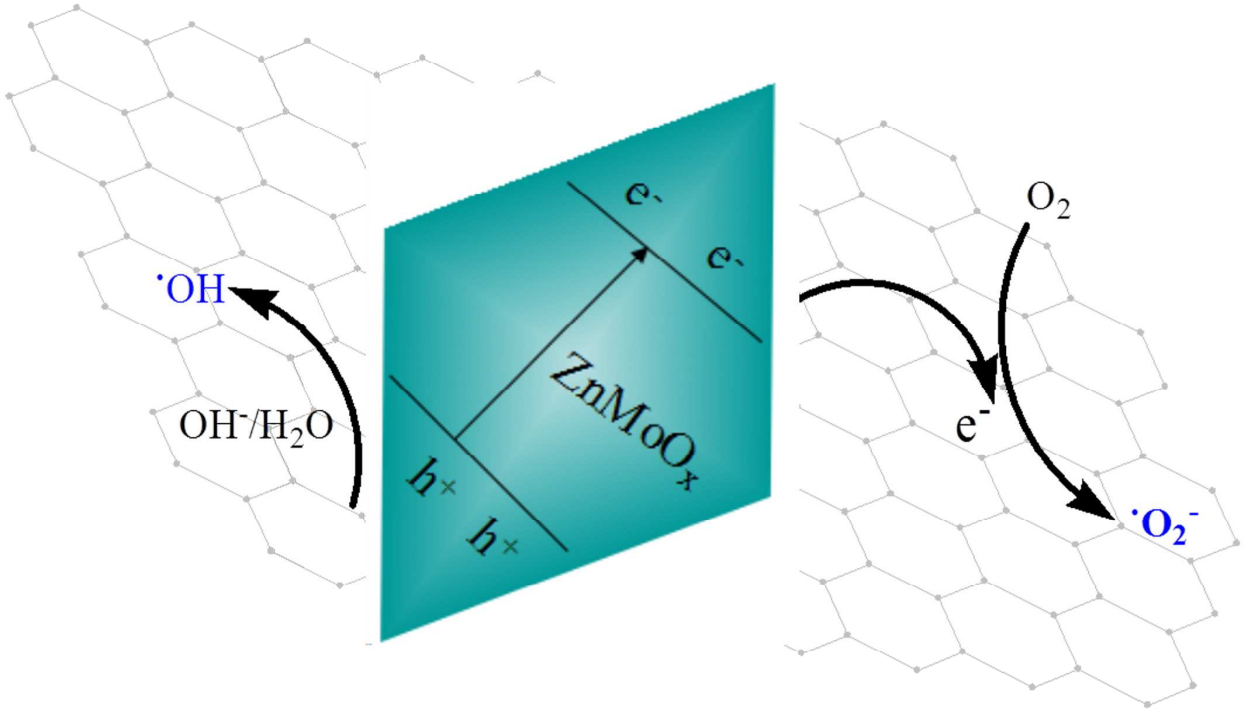

Fig. 6. Schematic illustration of the mechanism of charge transfer and photocatalytic process of RhB degradation over $ZnMoO_x$/RGO composites under natural sunlight irradiation.

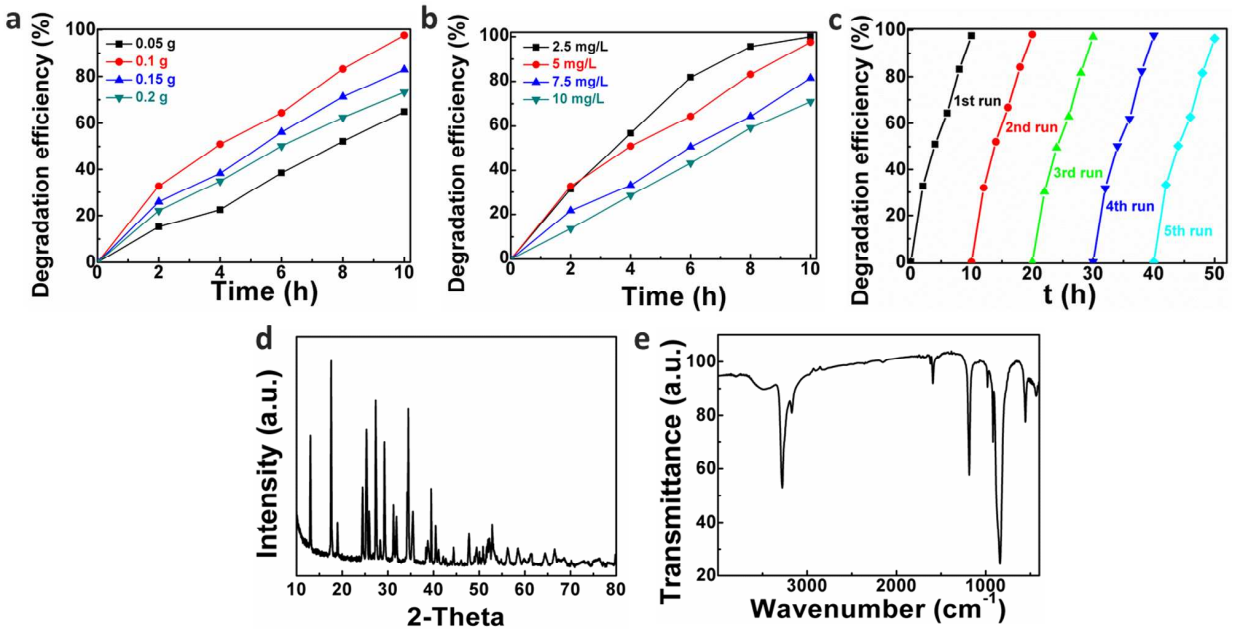

Fig. 7. The degradation efficiencies of the RhB solution by varying (a) the MG-3 dosage ([RhB] = 5 mg L^{-1}) and (b) the initial concentration of RhB ([MG-3] = 0.1 g) under natural sunlight irradiation. (c) Cycling photo-degradation of RhB-contained solution ([RhB] = 5 mg L^{-1}) using MG-3 (0.1 g) under natural sunlight irradiation. (d) XRD pattern and (e) FT-IR spectrum of the MG-3 experiencing the recycle experiment.

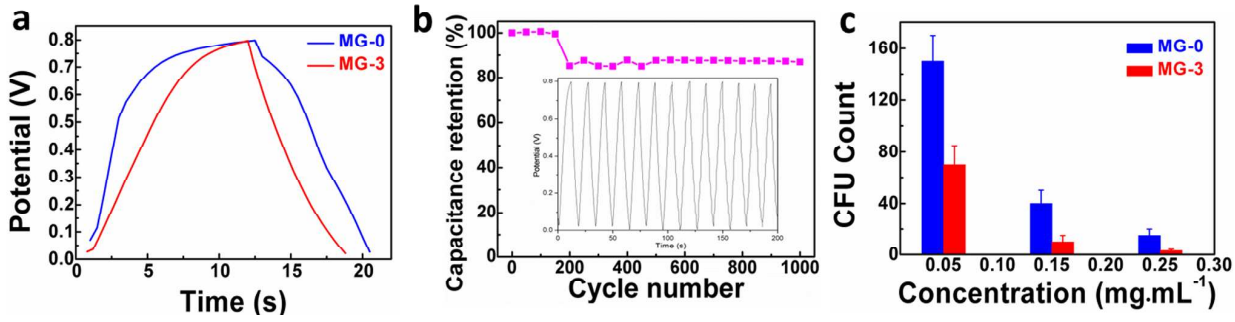

Fig. 8. (a) Galvanostatic charge/discharge curves of MG-0 and MG-3. (b) Cycle performance of the MG-3 measured at a current density of 0.1 mA cm^{-2}. The inset in (b) is the corresponding galvanostatic charge/discharge curve. (c) CFU counts of *E. coli* by using MG-0 and MG-3 as the culture medium.